

Strain-tunable in-plane ferroelectricity and lateral tunnel junction in monolayer group-IV monochalcogenides

Achintya Priyadarshi,¹ Yogesh Singh Chauhan,¹ Somnath Bhowmick,^{2,*} and Amit Agarwal^{3,†}

¹*Department of Electrical Engineering, Indian Institute of Technology, Kanpur, Kanpur 208016, India*

²*Department of Materials Science and Engineering,
Indian Institute of Technology, Kanpur, Kanpur 208016, India*

³*Department of Physics, Indian Institute of Technology, Kanpur, Kanpur 208016, India*

(Dated: January 24, 2022)

2D Ferroelectric materials are promising for designing low-dimensional memory devices. Here, we explore strain tunable ferroelectric properties of group-IV monochalcogenides MX (M=Ge, Sn; X=S, Se) and their potential application in lateral field tunnel junction devices. We find that these monolayers have in-plane ferroelectricity, with their ferroelectric parameters being on par with other known 2D ferroelectric materials. Amongst SnSe, SnS, GeSe, and GeS, we find that GeS has the best ferroelectric parameters for device applications, which can be improved further by applying uniaxial tensile strain. We use the calculated ferroelectric properties of these materials to study the tunneling electroresistance (TER) of a 4 nm device based on lateral ferroelectric tunnel junction. We find a substantial TER ratio $10^3 - 10^5$ in the devices based on these materials, which can be further improved up to a factor of 40 on the application of tensile strain.

I. INTRODUCTION

Conventional ferroelectrics (e.g., BaTiO₃ and PbTiO₃), possess switchable spontaneous electric polarization and large dielectric permittivity [1–3]. They are compatible with silicon-based devices [4] and offer intriguing functionality such as a giant tunneling electroresistance (TER) and negative capacitance (NC). Due to this, they have attracted significant interest in various applications such as random access memories (RAM), field-effect transistors (NCFET), sensors, and solar cells [5–10]. For exploring the possibility of ultralow-power, high-speed, and nanoscale memory devices in reduced dimensions, it is essential to retain the ferroelectricity of materials at the nanoscale and in reduced dimensions.

As a solution to these limitations, several two-dimensional ferroelectric materials (2D FEs) have been shown to display ferroelectric behaviour even in the monolayer limit of a few Å, and are attracting significant attention [11–17]. Some examples include SnTe [18], In₂Se₃ [19–21], group-V binary compounds [22], group-IV tellurides [23] and elemental group V monolayer [24]. An added advantage in 2D materials is the large strain-induced tunability of their electronic [25–27] and ferroelectric properties [28, 29]. However, several of these 2D FEs have relatively small spontaneous polarization and are not useful for device applications.

Recently, robust ferroelectricity with transition temperatures higher than the room temperature [30] has been found in Group-IV monochalcogenides MX (M=Ge, Sn; X=S, Se) thin films and dynamically stable MXs monolayers (ML) [31–33]. These MX thin films and ML also have a high thermoelectric performance, and

giant piezoelectricity [34, 35]. The in-plane ferroelectricity in these materials originates from the anharmonicity in their ionic potential. Moreover, the in-plane spontaneous polarization (P_s) is along the armchair direction and has a relatively larger value ($P_s = 1.56 - 4.88 \times 10^{-10}$ C/m) compared to other 2D FEs. These 2D FEs can be used to make a novel completely lateral in-plane ferroelectric tunnel junction (2D FTJ) based on p-type semiconductor/FE/n-type semiconductor structure [36]. These lateral 2D FTJ can display a giant TER of 1460%. Additionally, vertical 2D FE homojunction-based tunnel field-effect transistor (TFET) has been proposed to have low leakage current ($\sim 5-7 \mu A/\mu m$) for potential application in low power devices [37].

Motivated by these studies, here we explore strain tunability of in-plane ferroelectricity in group-IV monochalcogenides MX (M=Ge, Sn; X=S, Se) and lateral 2D FTJ devices based on them. We find that the value of spontaneous polarization and other ferroelectric parameters for these four MLs are relatively larger than most of the other known 2D materials, and the application of uniaxial strain can further enhance these. We also explore the performance of lateral FTJ based on these monolayers and show that GeSe and GeS display giant TER ($10^3 - 10^5$), with GeS having the largest value. The calculated TER value can be further increased by a factor of 40 under the application of 4% uniaxial tensile strain. Our study shows that these MX monolayers can be promising materials for 2D nonvolatile nanoscale devices such as lateral 2D FTJ.

The organization of the paper is as follows. Section II describes the crystal structure and computational details, and we discuss the in-plane ferroelectricity in these MX monolayers in Sec. III. The strain engineering of the ferroelectricity is discussed in Sec. IV, and the lateral field tunnel junction device and tunneling electroresistance are described in Sec. V. Our findings are summarized in Sec. VI.

* bsomnath@iitk.ac.in

† amitag@iitk.ac.in

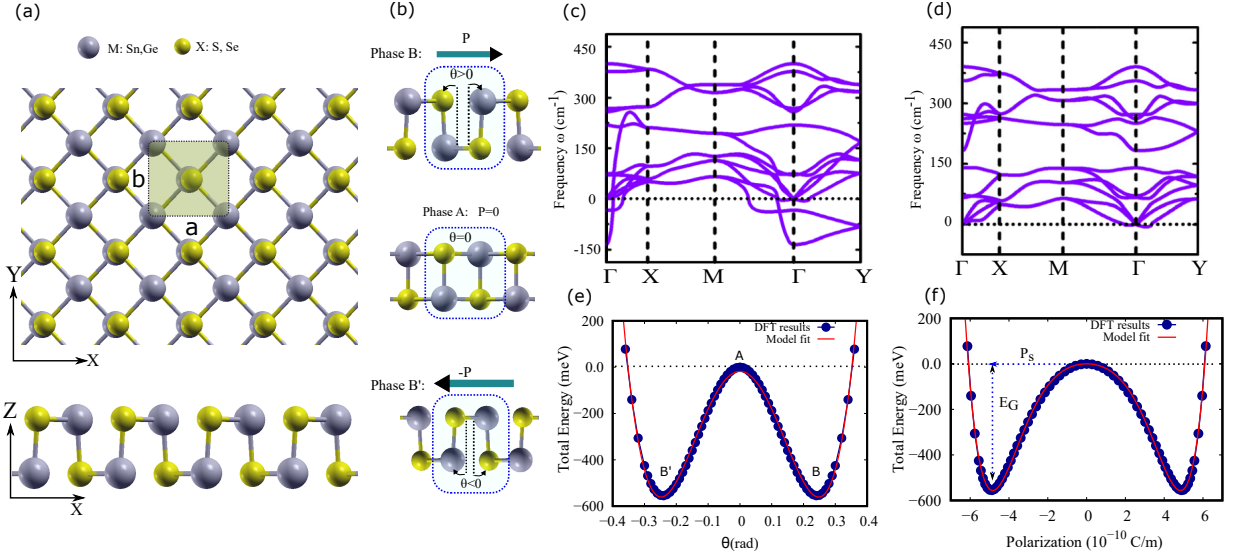


FIG. 1. (a) Top view and side view of MX monolayer crystal. The shaded rectangular region marks the unit cell, with a and b being the in-plane lattice constants along the armchair and zigzag direction, respectively. (b) Side view of the two degenerate non-centrosymmetric structures (ferroelectric phase B and B') and the centrosymmetric structure (paraelectric phase A). Phonon dispersion of monolayer GeS structures for the (c) A (unpolarized) phase and (d) B (polarized) phase. (e) Double-well potential as a function of the angular distortion (θ) of monolayer GeS. (f) Double-well potential as a function of the polarization of monolayer GeS. The spontaneous polarization and potential barrier are labeled as P_s and E_G , respectively. The fitting curve (red line) is based on the phenomenological Landau model.

II. COMPUTATIONAL DETAILS AND CRYSTAL STRUCTURE

The *ab initio* calculations are performed by density functional theory (DFT), using the projector-augmented wave pseudopotentials and a plane-wave basis set, as implemented in the Quantum Espresso package [38]. We treat electron exchange and correlation effects within the generalized gradient approximation (GGA) framework, proposed by the Perdew-Burke-Ernzerhof (PBE) [39, 40]. We use the Grimme-D2 [41] method to deal with dispersion forces. We set the kinetic energy cutoff to be 50 Ry for the plane-wave basis set and use a k -mesh of $14 \times 14 \times 1$ for the 2D Brillouin zone (BZ) integrations. We add a vacuum layer of 25 Å along the z -direction (perpendicular to the plane of the monolayer) to eliminate any interaction among the replica images. We carry out structural optimizations until all three components of the force on each atom are less than 0.01 eV/Å. We use XCRYSDEN [42] for preparing the crystal structures. We adopt the Berry phase method [43] to calculate the spontaneous ferroelectric polarization (P_s).

A representative crystal structure of the monolayer MX family ($M=\text{Sn, Ge}$; $X=\text{S, Se}$) is shown in Fig. 1(a). For SnSe, we have a rectangular unit cell with $a = 4.31$ Å, $b = 4.24$ Å, and it has four atoms per cell. Lattice parameters for other materials are reported in the Supporting Information [See Table S1]. As shown in Fig. 1(b), the para-electric (PE) phase (space group $Pmmn$) has an inversion symmetry (IS). The IS can be lifted by taking the Sn-Se bond along the z -direction and tilting it by an

angle $\pm\theta$, leading to the ferroelectric (FE) phase (space group $Pnm2_1$). Two such non-centrosymmetric structures are possible, namely the $B(\theta > 0)$ and $B'(\theta < 0)$ structures. Each structure can be continuously transformed to the other by spatial inversion [Fig. 1(b)], with the path passing via centrosymmetric phase $A(\theta = 0)$. Both B and B' have a polarization of the same magnitude but with opposite signs. Our calculations further reveal that the resultant polarization is an in-plane polarization, with the polarization axis being parallel to the x -direction, as marked in Fig. 1.

A comparison of the phonon spectra of PE and FE phase of GeS monolayer is shown in Fig. 1(c) and (d). While the ferroelectric phase has no negative frequencies, the paraelectric phase shows noticeable imaginary frequencies due to the soft optical modes. The existence of such soft phonon modes generally indicate a phase transition from a high symmetry centrosymmetric PE state to a low symmetry non-centrosymmetric FE state below some transition temperature T_c [44]. The phonon dispersion of the remaining monolayers are presented in Fig. S2 of the supplementary material, and they are found to be dynamically stable.

III. IN-PLANE FERROELECTRICITY IN MX

A unique feature of the spontaneous polarization in a material is the double well structure in the total energy as a function of the polarization. The double well potential for GeS is shown in Fig. 1(e) for energy vs. θ

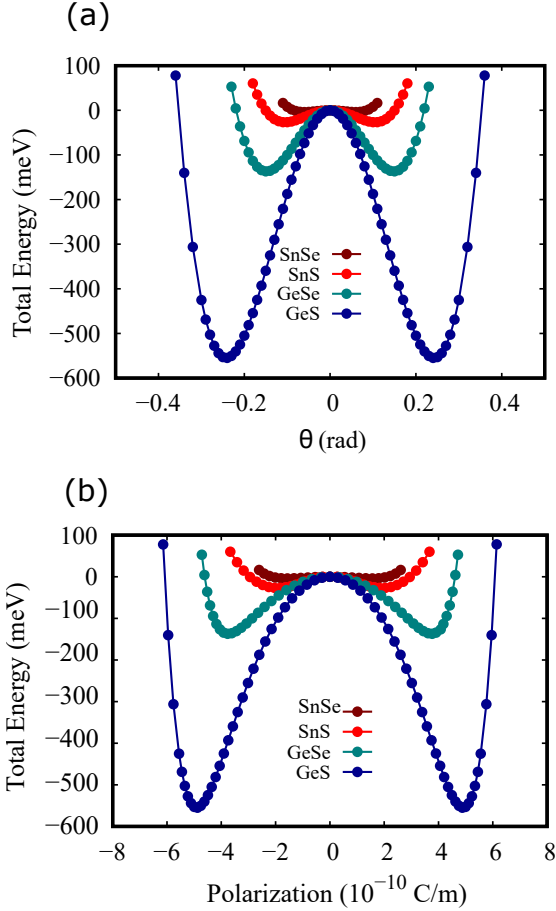


FIG. 2. (a) Double-well potential as a function of the angular distortion θ of monolayer SnSe, SnS, GeSe, and GeS. (b) Double-well potential as a function of polarization of monolayer SnSe, SnS, GeSe, and GeS. SnSe has the smallest P_s and E_G , whereas GeS has the largest P_s and E_G among the studied MX monolayers.

and in Fig. 1(f) for energy vs. polarization. The value of the spontaneous polarization and depth of the double well potential for GeS are found to be $P_s = 4.88 \times 10^{-10}$ C/m and $E_G = -554.85$ meV, respectively. Among the four MX monolayers considered here, SnSe (GeS) has the lowest (highest) P_s , as well as E_G values. In particular, GeS has E_G 137 times deeper than the corresponding SnSe value [Fig. 2 (a)]. Similarly, GeS has P_s 3 times larger than the corresponding SnSe value [Fig. 2 (b)]. We also calculated the saturation polarization (P_{sat}) of all four monolayers to explore their usefulness in memory applications such as FeFET. Monolayer GeS has the largest $P_{sat} = 6.14 \times 10^{-10}$ C/m, while SnSe has the lowest $P_{sat} = 2.61 \times 10^{-10}$ C/m among all four MXs. Taking advantage of larger P_{sat} , GeS can achieve a wider memory window and enhance the retention time of a FeFET based memory.

To understand the ferroelectricity in these materials better, we model the calculated polarization in these materials using the Landau Ginzburg (LG) theory. The LG

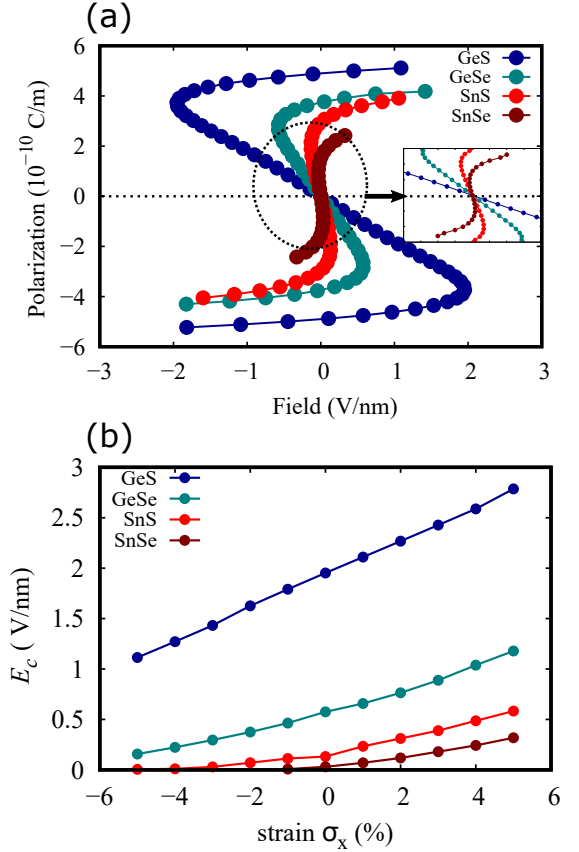


FIG. 3. (a) Polarization-field curve (or S-curve) obtained from the data of Fig. 2(b). (b) The strain dependence of the in-plane coercive field E_c of MX monolayers, calculated from S-curve.

model relates free energy (G) to polarization (P) via the relation [30, 45, 46]

$$G = \frac{A}{2}P^2 + \frac{B}{4}P^4 + \frac{C}{6}P^6. \quad (1)$$

We express G in units of meV per unit cell, and (P) in units of 10^{-10} C/m, respectively. The coefficients A , B and C are obtained by fitting Eq. 1 with the values obtained from *ab initio* calculations [Fig. 1(f)].

Another useful ferroelectric parameter is the coercive field E_c , the minimum electric field value needed to switch the polarization direction. In the steady state, the electric field dependence of the polarization (the “S” curve) is determined by the equation, $E = dG/dP$. Figure 3(a) shows the calculated S-curve of the four MX monolayers under strain-free conditions. The E_c can be calculated from the turning points of the S-curve, or $\frac{dE}{dP}|_{E=E_c} = 0$. We find that the E_c of GeS is largest, while that of SnSe is the smallest. Our calculated values of P_s and E_c are in good agreement with the previously reported theoretical values [30]. The experimental range of reported value of E_c in a monolayer SnSe is ~ 1.4 - 4.5×10^5 V/cm [47], which is in good agreement with our calculated value of $E_c \sim 3 \times 10^5$ V/cm. The polarization

TABLE I. The ground-state free energy (potential barrier) E_G (meV), spontaneous polarization P_s (10^{-10} C/m), saturation polarization P_{sat} (10^{-10} C/m), and Landau Ginzburg fitting parameters in Eq. (1), A , B , and C , which describe the double-well potential and the coercive field, E_c (V/nm). GeS has the largest spontaneous polarization.

Material	E_G	P_s	P_{sat}	A	B	C	E_c
SnSe	-4.049	1.564	2.608	-5.955	1.559	0.351	0.03
SnS	-26.741	2.036	3.666	-29.390	8.766	0.344	0.13
GeSe	-136.965	3.768	4.716	-15.434	-4.712	0.434	0.57
GeS	-554.845	4.877	6.142	-37.385	-5.787	0.315	1.95

parameters for all four monolayers are tabulated in Table I.

In 2D In_2Se_3 , the energy needed for the FE to PE transition is about 850 meV [48], which is considerably higher than that required in the studied monolayers. Since polarization switching has been demonstrated experimentally in In_2Se_3 [49, 50], we expect that the monolayers under consideration will also exhibit a polarization switching mechanism under appropriate experimental conditions.

A natural question to ask next is what happens to the ferroelectricity in these MX monolayers with strain, which we are going to discuss in the next section.

IV. STRAIN ENGINEERING OF FERROELECTRICITY IN MX

To explore the impact of uniaxial strain on the ferroelectricity, we apply a strain along the polar axis. The strain is introduced by changing the lattice parameter along the x -axis: $\sigma_x = (\frac{a-a_0}{a_0}) \times 100\%$, where a and a_0 are the lattice constants along x -direction for strained and unstrained unit cells, respectively. Experimentally this uniaxial strain can be achieved by various techniques such as using prestretched substrates, mismatch of thermal expansion, and bending flexible substrate [51–53]. The calculated phonon band structures of strained FE phase of considered monolayers are shown in Fig. S4 of the supplementary information. Importantly, these monolayers are found to be dynamically stable even at two extreme strain conditions. We find that tensile strain along the x -direction significantly enhances the polarization due to incremental change in the in-plane separation between the M (M=Ge,Sn) and the X (X=S,Se) atoms. This leads to an enhancement in the E_G and the P_s values. In contrast, compressive strain produces the opposite effect and decreases polarization [see Fig. S6 in the supplementary material].

The strain induced change in the free energy of SnSe is shown in Fig. 4(a) and (b) for variation of θ and the polarization, respectively. As shown in Fig. 4(a) and (b), the double well structure in the free energy disappears in SnSe and it becomes a paraelectric material under a relatively small compressive strain of 2%. On the other hand, tensile strain makes the potential well deeper and

increases the value of P_s . For example, we find that a 5% tensile strain enhances E_G by 17 times and P_s by 2 times, compared to the zero strain values of $E_G = -4.05$ meV and $P_s = 1.56 \times 10^{-10}$ C/m [Fig. 4(c) and (d)].

We find that the other MX monolayers show similar response under strain. However, the magnitude of compressive strain required for FE to PE conversion depends on the depth of the double well potential (E_G) of the pristine monolayer. For example, pristine SnS monolayer has a deeper potential ($E_G = -26.74$ meV) compared to pristine SnSe ($E_G = -4.05$ meV). As a result, SnS remains in the FE state up to $\sigma_x = -5\%$, while SnSe becomes a PE material at $\sigma_x = -2\%$. The variation of E_G and P_s with strain for all four MX monolayers is shown in Fig. 4(c) and (d), respectively. Since GeSe and GeS have even deeper potential well, having $E_G = -136.97$ meV and $E_G = -554.85$ meV, respectively, they do not undergo FE to PE transition up to compressive strain values of $\sigma_x = -5\%$ [Fig. 4(c)].

The strain induced change in the coercive field is shown in Fig. 3(b). We find that the coercive field is very sensitive to strain in all four MX monolayers, and it can change by upto 10 times for tensile strain upto 5%. The significant modulation of E_c of the MX monolayers due to applied strain can play a vital role in their potential applications in future electronics. As an example, for compressive strain in SnSe and SnS, the $V_c = E_c L < 2$ V (for $L = 20$ nm), which makes them potentially suitable for low power applications. We now explore the possibility of using the monolayer MX as 2D ferroelectrics tunnel junctions (FTJ).

V. LATERAL FIELD TUNNEL JUNCTION DEVICE AND TUNNELING ELECTRORESISTANCE

The four group IV MX monolayers displaying in-plane ferroelectricity can be used to make a lateral field tunnel junction (FTJ) device [36] out of the same material. This is in contrast to the generally vertical FTJ which use heterostructures with out of plane ferroelectric materials [54]. The lateral 2D FTJ device has an added advantage of being relatively easy to fabricate.

We explore the tunneling characteristics of the MX monolayer based homo-structural lateral FTJ device, as

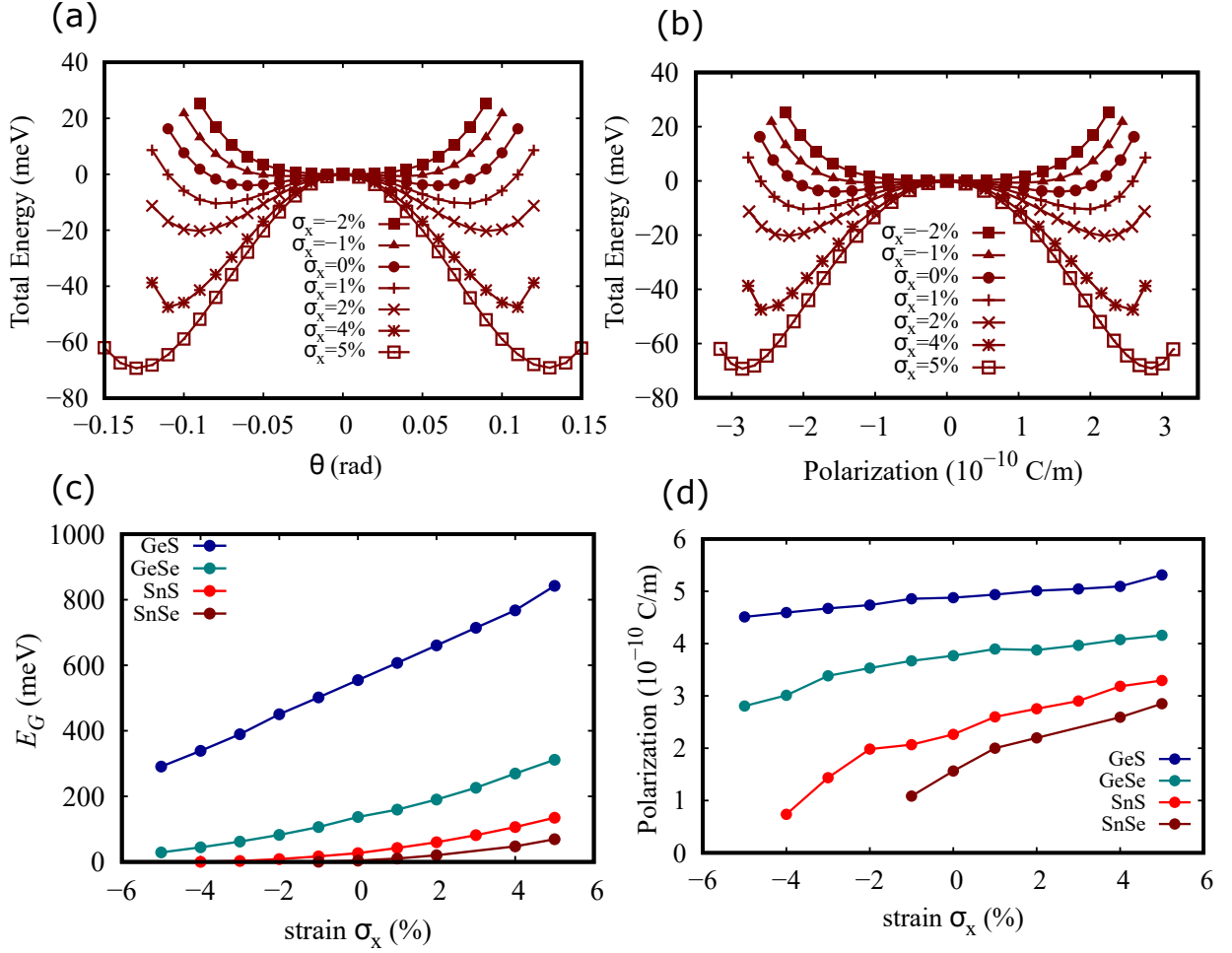


FIG. 4. Strain induced modification in the double-well potential as a function of (a) θ , (b) polarization for monolayer SnSe. At $\sigma_x = -2\%$, we find that E_G and $P_s = 0$ for SnSe, and the double well structure in the free energy disappears. (c) E_G and (d) P_s under the application of compressive and tensile strain.

shown in Fig. 5(a). The electrodes of the device are made of doped MX monochalcogenides (p-type or n-type) whereas as the MX ferroelectric layer is central region. Such a device can be thought to have two tunnel barriers, i) one arising from the mismatched doping in the two electrodes and the device region, and ii) an asymmetric and electrically switchable tunnel barrier arising from the direction of polarization in the ferroelectric material. The combination of these two tunneling barriers gives rise to the tunneling electroresistance (TER) effect [55].

The tunnel barrier arising from the mismatched doping in the two electrodes and the device part, can be modelled as a rectangular barrier of height U_0 with respect to the Fermi level E_F [5, 56]. The doping dependent values of U_0 can be evaluated from first principle calculations, and are listed in Table S2 for all MXs.

The ferroelectric tunnel barrier arises from the fact that the bound polarization charges at the interface are not completely screened by the adjacent electrodes. This leads to a non zero depolarizing fields in the ferroelec-

tric [57]. The magnitude and shape of the potential associated with this field depends on the magnitude and the direction of the polarization, as shown in Fig. 5(b). When the polarization is along the positive x -direction, (denoted as P_+) we have negative bound charges at the left interface and the positive bound charges at the right interface. Consequently holes are accumulated at the interface in the left electrode and electrons accumulate at the right electrode - see left panel of Fig. 5(a). For the polarization pointing towards negative x -axis (P_-), the situation is shown in the right panel of Fig. 5(a). This gives rise to an asymmetric potential profile depending on the polarization state of the ferroelectric.

The magnitude and shape of the of the electrostatic potential at the left and right interface is given by [5, 36, 58]

$$\phi_i = \pm \frac{\Gamma_i P_s d}{d + \epsilon_{FE}(\Gamma_L + \Gamma_R)}. \quad (2)$$

Here, $i = L/R$, P_s is the induced charge density at the interface of ferroelectric and electrode, and d is the length

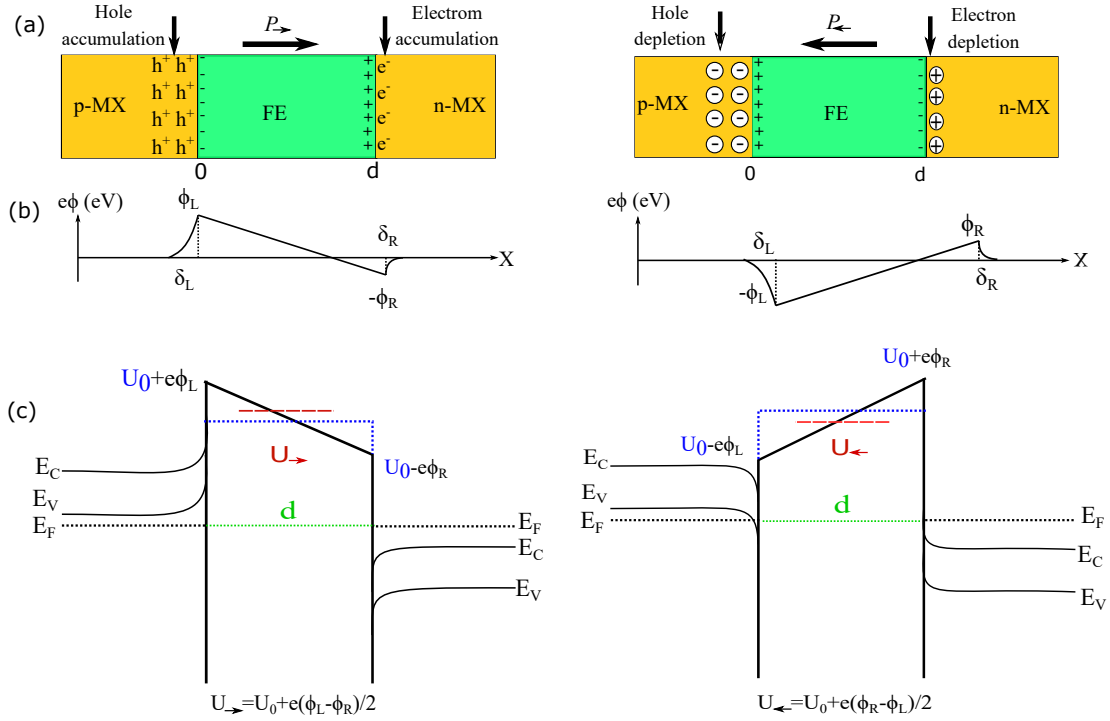


FIG. 5. Polarization reversal mechanisms in the 2D-field tunnel junction. (a) Schematic of the device in P_{\rightarrow} (left panel) and P_{\leftarrow} (right panel) states. The positive and negative bound charges in the FE region are shown by ‘+’ and ‘-’, respectively. The accumulated electrons and holes in doped regions are represented by ‘ e^- ’ and ‘ h^+ ’. The symbols ‘ \oplus ’ and ‘ \ominus ’ are used to show the depleted charges in doped regions. (b) Potential energy profile and screening length. (c) Band diagram and potential energy profile of the device. Dotted red line shows the average potential barrier height for two cases, taking E_F as a reference.

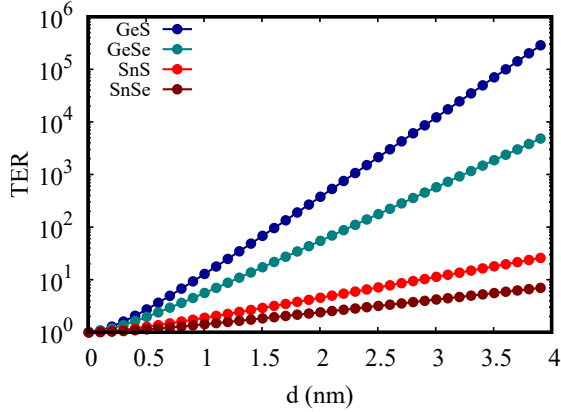


FIG. 6. TER as a function of 2D ferroelectric barrier width at zero strain. The parameters used to calculate TER are listed in Table S2.

of the central region, and ϵ_{FE} is the dielectric constant of the ferroelectric. In Eq. (2), $\Gamma_i = \delta_i/\epsilon_i$ is the ratio of the screening length of the electrode i with its dielectric permittivity ϵ_i . The screening length δ of a given electrode can be estimated from the Thomas Fermi model. It is given by $\delta = \frac{1}{e} \sqrt{\epsilon/\rho(E_F)}$ where $\rho(E_F)$ is the density of states (DOS) at Fermi energy. In our homo-structural device, we have $\epsilon_i = \epsilon_{FE}$. Thus, the screening length

of the electrode depends on $\rho(E_F)$ only, and it can be tuned by the doping of the electrode. In our device the left (right) electrode is p -doped (n -doped) and hence we have $\delta_L > \delta_R$, or $\Gamma_L > \Gamma_R$.

Combining both these potential barriers, we have $U_{\rightarrow} = U_0 + e(\phi_L - \phi_R)/2$ for the P_{\rightarrow} state and $U_{\leftarrow} = U_0 + e(\phi_R - \phi_L)/2$ for the P_{\leftarrow} state, respectively [59, 60]. The modulation of the asymmetric trapezoidal tunnel barrier due to the reversal of polarization changes the tunneling conductance, G . This gives rise to a finite TER ratio, defined as $TER = (G_{\rightarrow} - G_{\leftarrow})/G_{\leftarrow}$, for small applied voltages. A simple estimate for the TER ratio can be done via the Wentzel-Kramers-Brillouin (WKB) approximation for the tunneling probability. This generally works well for $d\sqrt{2m\phi_{1/2}} \gg \hbar$.

Using the WKB approximation, in the linear response regime, for $\Delta U = U_{\rightarrow} - U_{\leftarrow} \ll U_0$, the TER can be expressed as [61, 62]

$$TER \approx \left[\frac{\sqrt{2m}\Delta U}{\hbar\sqrt{U_0}} \right] = \exp \left[\frac{e}{\hbar} \sqrt{\frac{2m}{U_0}} \frac{P_s (\Gamma_L - \Gamma_R) d^2}{d + \epsilon_{FE}(\Gamma_L + \Gamma_R)} \right]. \quad (3)$$

Here, m is the effective mass of the carrier in the barrier region. The TER ratio calculated using Eq. (3) is shown in Fig. 6 for all four MX monolayers. From Fig. 5 (c), it can be clearly seen that the average tunneling barrier in

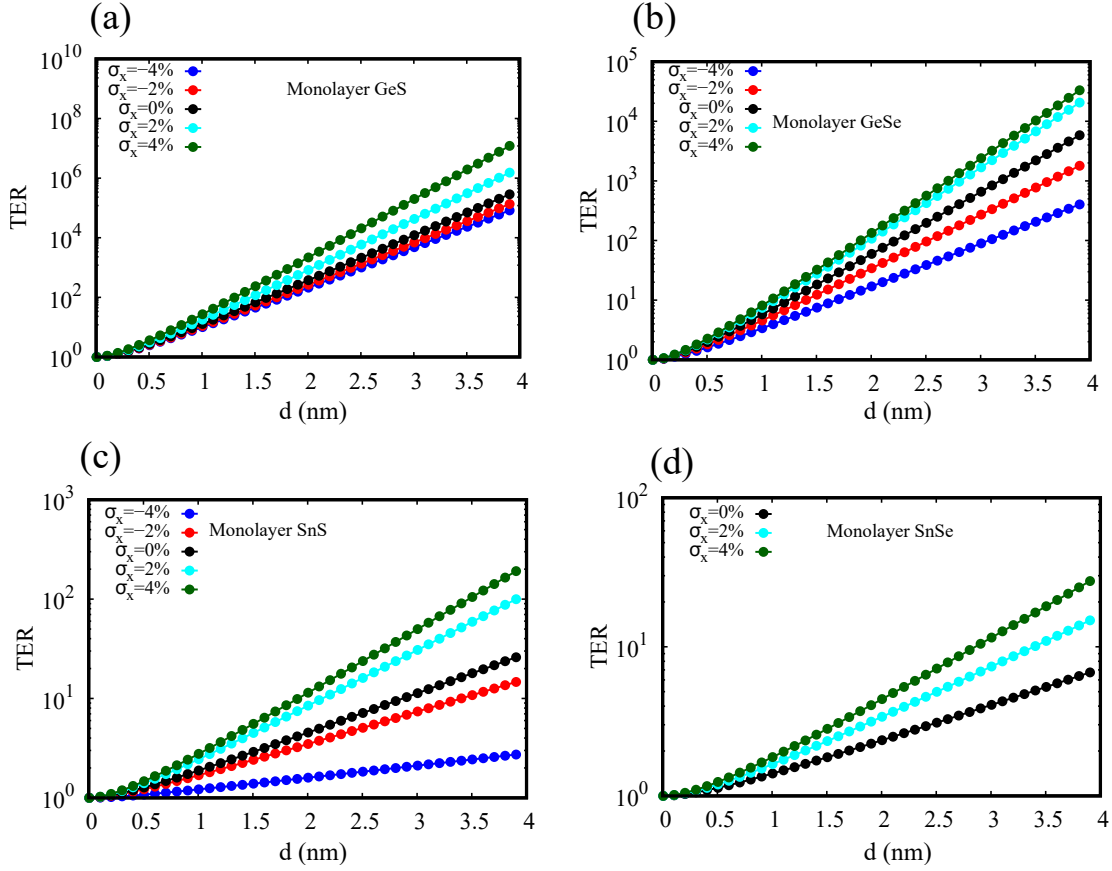


FIG. 7. Strain dependence of TER for (a) GeS, (b) GeSe, (c) SnS and (d) SnSe monolayers.

the P_{\rightarrow} state is larger for as compared to P_{\leftarrow} state. Thus, the conductance G_{\rightarrow} decays faster than G_{\leftarrow} with increasing width d , causing the TER to increase exponentially with the width. We find that for a 4 nm device, SnSe and SnS have a TER ratio of 10 and 26, respectively, while the other two MX monolayers (GeS, GeSe) have a relatively large TER $10^3 - 10^5$. One reason for this is that $\text{TER} \propto \exp[P_s]$, and SnSe has the lowest P_s among all four monolayers. Note that while the TER seems to have an explicit dependence on the effective mass, it is cancelled by the $\Gamma \propto \sqrt{1/\rho(E_F)} \propto 1/\sqrt{m}$ term. We find that for a 4 nm device, the value of TER in GeS and GeSe, is significantly larger than that reported in SnTe based in-plane FJT [63] which has a $\text{TER} \approx 10^2$. Thus, our calculations suggest GeS and GeSe to be good potential candidates for exploring TER based memory devices.

The variation of P_s with strain (see Fig. 4), also manifests in the strain modulation of TER, as shown in Fig. 7. We find that the ratio of the screening lengths in the two electrodes $\delta_L/\delta_R \approx 2$ for all four MX monolayers. Further this ratio does not change by much with applied strain. Thus the strain modulation of the TER predominantly arises from the P_s . However, the applied strain markedly modulates P_s and hence TER. We find that under tensile strain of upto $\sigma_x = -4\%$, the TER can increase upto a factor of 40, while a compressive strain of

$\sigma_x = 4\%$ decreases the TER value by 4 times as compared to the unstrained case.

VI. CONCLUSION

In conclusion, we have systematically demonstrated the existence and strain tunability of intrinsic in-plane ferroelectricity in monolayer group-IV monochalcogenides MX (M=Ge, Sn; X=S, Se), using the first-principles DFT calculations. We show that GeS has the largest spontaneous polarization value while SnSe has the lowest value amongst the four MX monolayers. The spontaneous polarization values of GeS are comparable to the largest polarization value reported in other 2D ferroelectric materials such as SbN and BiP [29]. We find that the tensile strain increases the remnant polarization and E_G in all four monolayers, while the compressive strain decreases it.

Additionally, we demonstrate the applicability of these 4 monolayers in lateral field tunnel junction devices. We find that GeS, and GeSe have a large TER ratio of $10^3 - 10^5$ making them excellent candidate materials for lateral FTJ devices. Tensile strain of upto 4% can increase the TER in these materials by a factor of 40. Our study will open up further avenues for exploration of fundamental

physics and device applications based on the interplay between ferroelectricity and mechanical, electronic and optical properties in these MX monolayers.

SUPPLEMENTARY MATERIAL

See the supplementary material for (i) the electronic band structure of MX monolayers, (ii) the dynamical stability of SnSe, GeSe and SnS monolayers, (iii) polar modes in all MX monolayers, (iv) phonon dispersion of monolayers at two extreme strain conditions, (v) strain-induced modification in the double-well potential of GeS, GeSe, and SnS monolayers, (vi) the change in the in-plane separation of MX atoms as a function of strain σ_x , and polarization as a function of in-plane separation, (vii) the strain dependence of S-curve, (viii) the strain dependence of the coercive voltage V_c , and (ix) relevant parameters of pristine monochalcogenides used in TER calculation.

ACKNOWLEDGEMENTS

We acknowledge financial support by the Swarna-jayanti Fellowship (Grant No. DST/SJF/ETA-02/2017-

18), the FIST Scheme (Grant No. SR/FST/ETII-072/2016) of the Department of Science and Technology, India, the Berkeley Device Modeling Center and the Science and Engineering Research Board, India (Grant No. EMR/2017/004970). We acknowledge National Supercomputing Mission (NSM) for providing computing resources of “PARAM Sanganak” at IIT Kanpur, which is implemented by C-DAC and supported by the Ministry of Electronics and Information Technology (MeitY) and Department of Science and Technology (DST), Government of India. We also acknowledge the HPC facility provided by CC, IIT Kanpur.

CONFLICT OF INTEREST

The authors declare no conflict of interest.

DATA AVAILABILITY STATEMENT

The data that support the findings of this study are available from the corresponding author upon reasonable request.

-
- [1] G. Burns and B. A. Scott, Lattice modes in ferroelectric perovskites: Pbtio₃, *Phys. Rev. B* **7**, 3088 (1973)
 - [2] S. Wemple, M. Didomenico, and I. Camlibel, Dielectric and optical properties of melt-grown batio₃, *Journal of Physics and Chemistry of Solids* **29**, 1797 (1968)
 - [3] W. J. Merz, Switching time in ferroelectric batio₃ and its dependence on crystal thickness, *Journal of Applied Physics* **27**, 938 (1956)
 - [4] R. A. McKee, F. J. Walker, and M. F. Chisholm, Crystalline oxides on silicon: The first five monolayers, *Phys. Rev. Lett.* **81**, 3014 (1998)
 - [5] M. Y. Zhuravlev, R. F. Sabirianov, S. S. Jaswal, and E. Y. Tsybmal, Giant electroresistance in ferroelectric tunnel junctions, *Phys. Rev. Lett.* **94**, 246802 (2005)
 - [6] Z. Wang, H. Li, H. Hu, Y. Fan, R. Fan, B. Li, J. Zhang, H. Liu, J. Fan, H. Hou, F. Dang, Z. Kou, and Z. Guo, Direct observation of stable negative capacitance in sr-tio₃@batio₃ heterostructure, *Advanced Electronic Materials* **6**, 1901005 (2020)
 - [7] Z. Yan, Y. Guo, G. Zhang, and J.-M. Liu, High-performance programmable memory devices based on co-doped batio₃, *Advanced Materials* **23**, 1351 (2011)
 - [8] A. I. Khan, C. W. Yeung, Chenming Hu, and S. Salahuddin, Ferroelectric negative capacitance mosfet: Capacitance tuning antiferroelectric operation, in *2011 International Electron Devices Meeting* (2011) pp. 11.3.1–11.3.4
 - [9] W. Wang, F. Liu, C. Man Lau, L. Wang, G. Yang, D. Zheng, and Z. Li, Field-effect batio₃-si solar cells, *Applied Physics Letters* **104**, 123901 (2014)
 - [10] M. Hoffmann, F. P. Fengler, M. Herzig, T. Mittmann, B. Max, U. Schroeder, R. Negrea, P. Lucian, S. Slesazeck, and T. Mikolajick, Unveiling the double-well energy landscape in a ferroelectric layer, *Nature* **565**, 464 (2019)
 - [11] S. N. Shirodkar and U. V. Waghmare, Emergence of ferroelectricity at a metal-semiconductor transition in a 1t monolayer of mos₂, *Phys. Rev. Lett.* **112**, 157601 (2014)
 - [12] M. Osada and T. Sasaki, The rise of 2d dielectrics/ferroelectrics, *APL Materials* **7**, 120902 (2019)
 - [13] L. Qi, S. Ruan, and Y.-J. Zeng, Review on recent developments in 2d ferroelectrics: Theories and applications, *Advanced Materials* **33**, 2005098 (2021)
 - [14] A. Chandrasekaran, A. Mishra, and A. K. Singh, Ferroelectricity, antiferroelectricity, and ultrathin 2d electron/hole gas in multifunctional monolayer mxene, *Nano letters* **17**, 3290 (2017)
 - [15] C. Cui, F. Xue, W.-J. Hu, and L.-J. Li, Two-dimensional materials with piezoelectric and ferroelectric functionalities, *npj 2D Materials and Applications* **2**, 1 (2018)
 - [16] J. Shang, X. Tang, and L. Kou, Two dimensional ferroelectrics: Candidate for controllable physical and chemical applications, *Wiley Interdisciplinary Reviews: Computational Molecular Science* **11**, e1496 (2021)
 - [17] M. Liu, T. Liao, Z. Sun, Y. Gu, and L. Kou, 2d ferroelectric devices: working principles and research progress, *Physical Chemistry Chemical Physics* **23**, 21376 (2021)
 - [18] K. Chang, J. Liu, H. Lin, N. Wang, K. Zhao, A. Zhang, F. Jin, Y. Zhong, X. Hu, W. Duan, Q. Zhang, L. Fu, Q.-K. Xue, X. Chen, and S.-H. Ji, Discovery of robust in-plane ferroelectricity in atomic-thick snse, *Science* **353**,

- 274 (2016)
- [19] M. Soleimani and M. Pourfath, Ferroelectricity and phase transitions in in 2 se 3 van der waals material, *Nanoscale* **12**, 22688 (2020)
 - [20] C. Xu, Y. Chen, X. Cai, A. Meingast, X. Guo, F. Wang, Z. Lin, T. W. Lo, C. Maunders, S. Lazar, N. Wang, D. Lei, Y. Chai, T. Zhai, X. Luo, and Y. Zhu, Two-dimensional antiferroelectricity in nanostripe-ordered in_2se_3 , *Phys. Rev. Lett.* **125**, 047601 (2020)
 - [21] J. Ding, D.-F. Shao, M. Li, L.-W. Wen, and E. Y. Tsymbal, Two-dimensional antiferroelectric tunnel junction, *Phys. Rev. Lett.* **126**, 057601 (2021)
 - [22] D. Di Sante, A. Stroppa, P. Barone, M.-H. Whangbo, and S. Picozzi, Emergence of ferroelectricity and spin-valley properties in two-dimensional honeycomb binary compounds, *Phys. Rev. B* **91**, 161401 (2015)
 - [23] W. Wan, C. Liu, W. Xiao, and Y. Yao, Promising ferroelectricity in 2d group iv tellurides: a first-principles study, *Applied Physics Letters* **111**, 132904 (2017)
 - [24] C. Xiao, F. Wang, S. A. Yang, Y. Lu, Y. Feng, and S. Zhang, Elemental ferroelectricity and antiferroelectricity in group-v monolayer, *Advanced Functional Materials* **28**, 1707383 (2018)
 - [25] X. Peng, Q. Wei, and A. Copple, Strain-engineered direct-indirect band gap transition and its mechanism in two-dimensional phosphorene, *Phys. Rev. B* **90**, 085402 (2014)
 - [26] R. Fei and L. Yang, Strain-engineering the anisotropic electrical conductance of few-layer black phosphorus, *Nano letters* **14**, 2884 (2014)
 - [27] A. Priyadarshi, Y. S. Chauhan, S. Bhowmick, and A. Agarwal, Strain-tunable charge carrier mobility of atomically thin phosphorus allotropes, *Phys. Rev. B* **97**, 115434 (2018)
 - [28] J. Haeni, P. Irvin, W. Chang, R. Uecker, P. Reiche, Y. Li, S. Choudhury, W. Tian, M. Hawley, B. Craigo, *et al.*, Room-temperature ferroelectricity in strained srTiO_3 , *Nature* **430**, 758 (2004)
 - [29] C. Liu, W. Wan, J. Ma, W. Guo, and Y. Yao, Robust ferroelectricity in two-dimensional sb_2Te_3 and bi_2Te_3 , *Nanoscale* **10**, 7984 (2018)
 - [30] R. Fei, W. Kang, and L. Yang, Ferroelectricity and phase transitions in monolayer group-iv monochalcogenides, *Phys. Rev. Lett.* **117**, 097601 (2016)
 - [31] L. Li, Z. Chen, Y. Hu, X. Wang, T. Zhang, W. Chen, and Q. Wang, Single-layer single-crystalline snse nanosheets, *Journal of the American Chemical Society* **135**, 1213 (2013)
 - [32] Z. Hu, Y. Ding, X. Hu, W. Zhou, X. Yu, and S. Zhang, Recent progress in 2d group IV–IV monochalcogenides: synthesis, properties and applications, *Nanotechnology* **30**, 252001 (2019)
 - [33] G. Qin, Z. Qin, W.-Z. Fang, L.-C. Zhang, S.-Y. Yue, Q.-B. Yan, M. Hu, and G. Su, Diverse anisotropy of phonon transport in two-dimensional group iv–vi compounds: A comparative study, *Nanoscale* **8**, 11306 (2016)
 - [34] Z.-Y. Hu, K.-Y. Li, Y. Lu, Y. Huang, and X.-H. Shao, High thermoelectric performances of monolayer snse allotropes, *Nanoscale* **9**, 16093 (2017)
 - [35] L. C. Gomes, A. Carvalho, and A. H. Castro Neto, Enhanced piezoelectricity and modified dielectric screening of two-dimensional group-iv monochalcogenides, *Phys. Rev. B* **92**, 214103 (2015)
 - [36] X.-W. Shen, Y.-W. Fang, B.-B. Tian, and C.-G. Duan, Two-dimensional ferroelectric tunnel junction: the case of monolayer in_2se_3 , *ACS Applied Electronic Materials* **1**, 1133 (2019)
 - [37] H. Li, J. Liang, P. Xu, J. Luo, and F. Liu, Vertically stacked snse homojunctions and negative capacitance for fast low-power tunneling transistors, *RSC Adv.* **10**, 20801 (2020)
 - [38] P. Giannozzi, S. Baroni, N. Bonini, M. Calandra, R. Car, C. Cavazzoni, D. Ceresoli, G. L. Chiarotti, M. Cococcioni, I. Dabo, A. D. Corso, S. de Gironcoli, S. Fabris, G. Fratesi, R. Gebauer, U. Gerstmann, C. Gougousis, A. Kokalj, M. Lazzeri, L. Martin-Samos, N. Marzari, F. Mauri, R. Mazzarello, S. Paolini, A. Pasquarello, L. Paulatto, C. Sbraccia, S. Scandolo, G. Sclauzero, A. P. Seitsonen, A. Smogunov, P. Umari, and R. M. Wentzcovitch, QUANTUM ESPRESSO: a modular and open-source software project for quantum simulations of materials, *Journal of Physics: Condensed Matter* **21**, 395502 (2009)
 - [39] J. P. Perdew and A. Zunger, Self-interaction correction to density-functional approximations for many-electron systems, *Phys. Rev. B* **23**, 5048 (1981)
 - [40] P. E. Blöchl, Projector augmented-wave method, *Phys. Rev. B* **50**, 17953 (1994)
 - [41] S. Grimme, Semiempirical gga-type density functional constructed with a long-range dispersion correction, *Journal of Computational Chemistry* **27**, 1787 (2006)
 - [42] A. Kokalj, Computer graphics and graphical user interfaces as tools in simulations of matter at the atomic scale, *Computational Materials Science* **28**, 155 (2003), proceedings of the Symposium on Software Development for Process and Materials Design
 - [43] R. D. King-Smith and D. Vanderbilt, Theory of polarization of crystalline solids, *Phys. Rev. B* **47**, 1651 (1993)
 - [44] P. A. Fleury, J. F. Scott, and J. M. Worlock, Soft phonon modes and the 110°k phase transition in srTiO_3 , *Phys. Rev. Lett.* **21**, 16 (1968)
 - [45] A. D. Bruce, Structural phase transitions. ii. static critical behaviour, *Advances in Physics* **29**, 111 (1980)
 - [46] J. C. Wojdel and J. Íñiguez, Testing simple predictors for the temperature of a structural phase transition, *Phys. Rev. B* **90**, 014105 (2014)
 - [47] K. Chang, F. Küster, B. J. Miller, J.-R. Ji, J.-L. Zhang, P. Sessi, S. Barraza-Lopez, and S. S. P. Parkin, Microscopic manipulation of ferroelectric domains in snse monolayers at room temperature, *Nano Letters* **20**, 6590 (2020)
 - [48] W. Ding, J. Zhu, Z. Wang, Y. Gao, D. Xiao, Y. Gu, Z. Zhang, and W. Zhu, Prediction of intrinsic two-dimensional ferroelectrics in in 2 se 3 and other iii 2-vi 3 van der waals materials, *Nature communications* **8**, 1 (2017)
 - [49] C. Cui, W.-J. Hu, X. Yan, C. Addiego, W. Gao, Y. Wang, Z. Wang, L. Li, Y. Cheng, P. Li, *et al.*, Intercorrelated in-plane and out-of-plane ferroelectricity in ultrathin two-dimensional layered semiconductor in_2se_3 , *Nano letters* **18**, 1253 (2018)
 - [50] H. Ryu, K. Xu, D. Li, X. Hong, and W. Zhu, Empowering 2d nanoelectronics via ferroelectricity, *Applied Physics Letters* **117**, 080503 (2020)
 - [51] S. Yang, Y. Chen, and C. Jiang, Strain engineering of two-dimensional materials: Methods, properties, and ap-

- plications, [InfoMat](#) **3**, 397 (2021)
- [52] Z. Li, Y. Lv, L. Ren, J. Li, L. Kong, Y. Zeng, Q. Tao, R. Wu, H. Ma, B. Zhao, *et al.*, Efficient strain modulation of 2d materials via polymer encapsulation, [Nature communications](#) **11**, 1 (2020)
 - [53] Y. Sun and K. Liu, Strain engineering in functional 2-dimensional materials, [Journal of Applied Physics](#) **125**, 082402 (2019)
 - [54] V. Garcia and M. Bibes, Ferroelectric tunnel junctions for information storage and processing, [Nature communications](#) **5**, 1 (2014)
 - [55] E. Y. Tsymbal and H. Kohlstedt, Tunneling across a ferroelectric, [Science](#) **313**, 181 (2006)
 - [56] Z. Wen, C. Li, D. Wu, A. Li, and N. Ming, Ferroelectric-field-effect-enhanced electroresistance in metal/ferroelectric/semiconductor tunnel junctions, [Nature materials](#) **12**, 617–621 (2013)
 - [57] R. R. Mehta, B. D. Silverman, and J. T. Jacobs, Depolarization fields in thin ferroelectric films, [Journal of Applied Physics](#) **44**, 3379 (1973)
 - [58] J. Velez, J. Burton, M. Y. Zhuravlev, and E. Tsymbal, [Predictive modelling of ferroelectric tunnel junctions](#) (2016)
 - [59] J. G. Simmons, Generalized formula for the electric tunnel effect between similar electrodes separated by a thin insulating film, [Journal of Applied Physics](#) **34**, 1793 (1963)
 - [60] W. F. Brinkman, R. C. Dynes, and J. M. Rowell, Tunneling conductance of asymmetrical barriers, [Journal of Applied Physics](#) **41**, 1915 (1970)
 - [61] A. Gruverman, D. Wu, H. Lu, Y. Wang, H. Jang, C. Folkman, M. Y. Zhuravlev, D. Felker, M. Rzchowski, C.-B. Eom, *et al.*, Tunneling electroresistance effect in ferroelectric tunnel junctions at the nanoscale, [Nano letters](#) **9**, 3539 (2009)
 - [62] A. Sokolov, O. Bak, H. Lu, S. Li, E. Y. Tsymbal, and A. Gruverman, Effect of epitaxial strain on tunneling electroresistance in ferroelectric tunnel junctions, [Nanotechnology](#) **26**, 305202 (2015)
 - [63] H. Shen, J. Liu, K. Chang, and L. Fu, In-plane ferroelectric tunnel junction, [Phys. Rev. Applied](#) **11**, 024048 (2019)

Supporting Information for
Strain-tunable in-plane ferroelectricity and lateral tunnel junction in
monolayer group-IV monochalcogenides

Achintya Priyadarshi,¹ Yogesh Singh Chauhan,¹ Somnath Bhowmick,^{2,*} and Amit Agarwal^{3,†}

¹*Department of Electrical Engineering, Indian Institute of Technology, Kanpur, Kanpur 208016, India*

²*Department of Materials Science and Engineering,
Indian Institute of Technology, Kanpur, Kanpur 208016, India*

³*Department of Physics, Indian Institute of Technology, Kanpur, Kanpur 208016, India*

(Dated: January 24, 2022)

* bsomnath@iitk.ac.in

† amitag@iitk.ac.in

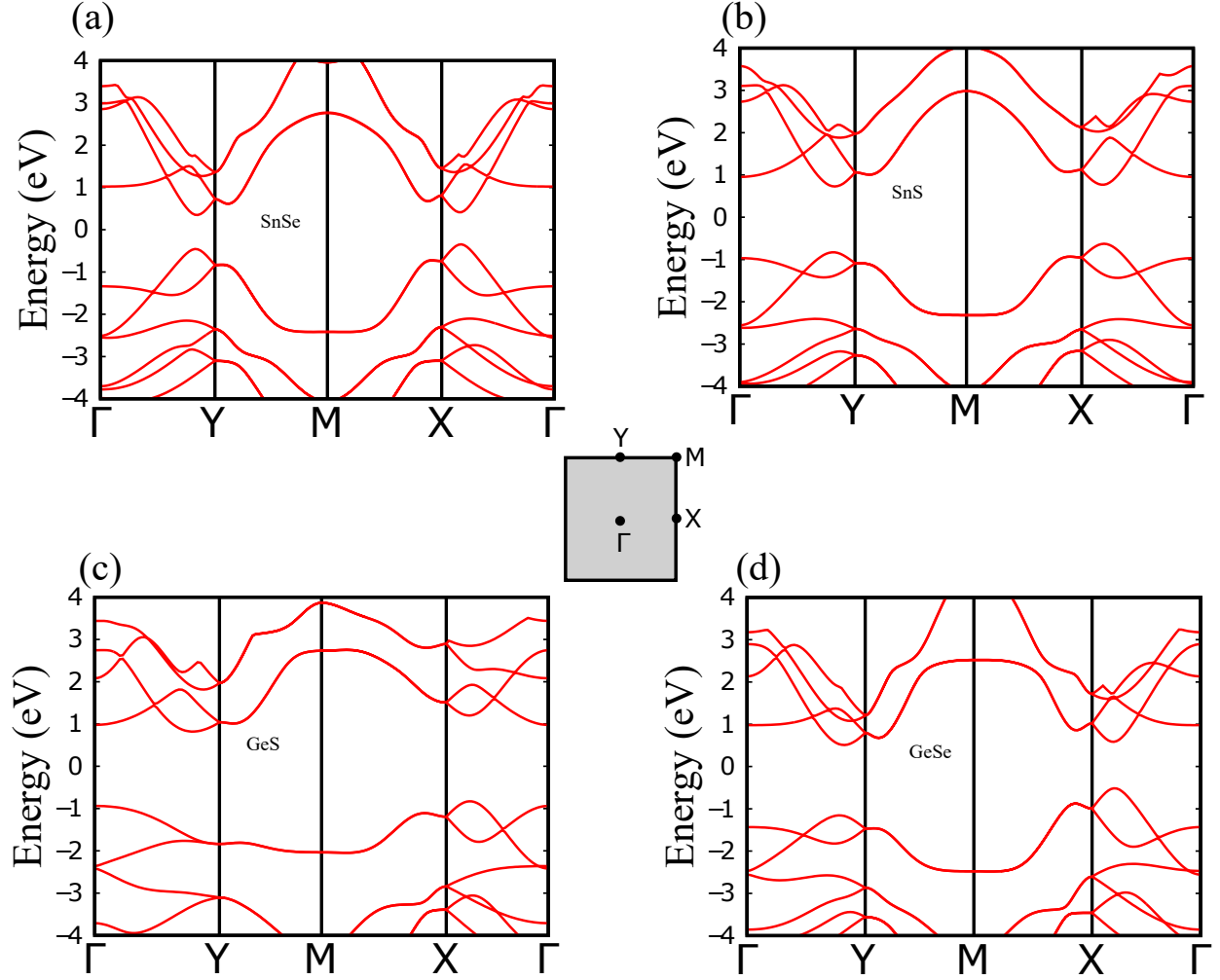


FIG. S1: DFT-PBE calculated electronic band structure of (a) SnSe, (b) SnS, (c) GeS, and (d) GeSe monolayers. The shaded rectangular region represents the Brillouin zone.

TABLE S1: DFT-PBE calculated band gap and lattice parameters of MX monolayers.

Material:	SnSe	SnS	GeSe	GeS
$E_g(\text{eV})$	0.70	1.35	1.02	1.65
$ a $ (\AA)	4.31	4.20	4.27	4.47
$ b $ (\AA)	4.24	4.06	3.92	3.62

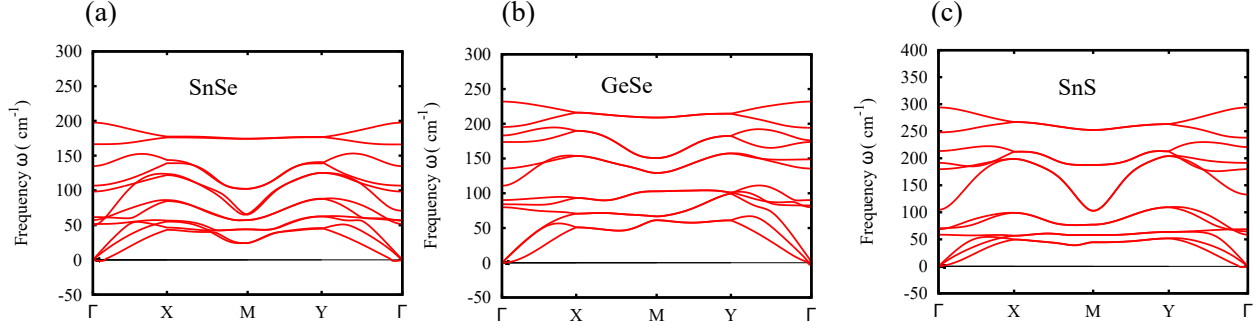


FIG. S2: Phonon band structure of a) SnSe, b) GeSe, and c) SnS monolayer without strain.

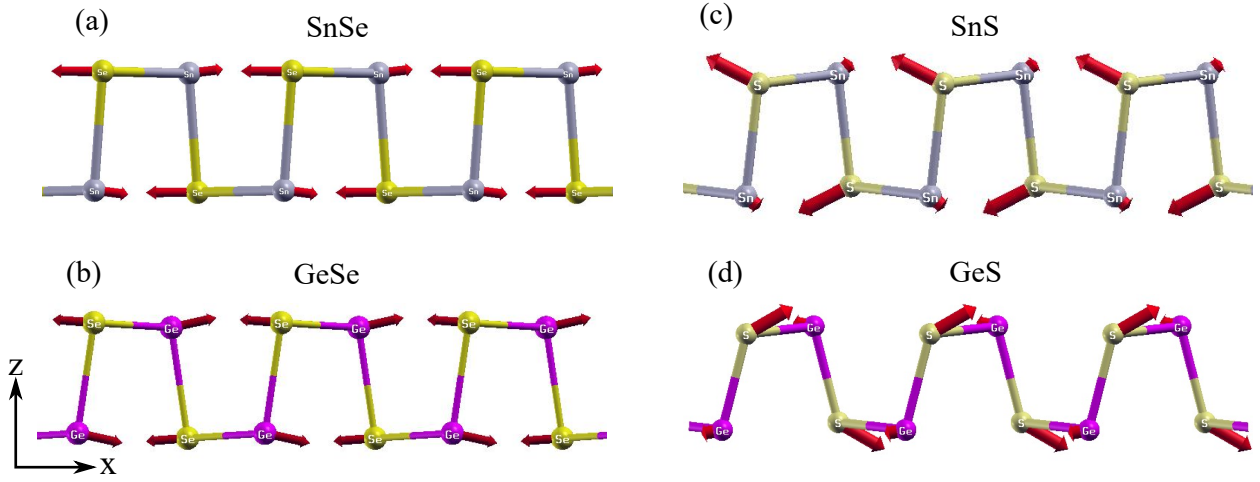


FIG. S3: Polar vibrational modes responsible for spontaneous polarization in (a) SnSe, (b) GeSe, (c) SnS, and (d) GeS monolayer at Γ point.

TABLE S2: Carrier effective mass and other relevant parameters of pristine monochalcogenides needed in TER calculation.

Material:	m^*/m_0	ϵ_{FE}/ϵ_0	$U_0(eV)$	$\delta_{L,R}(\text{\AA})$
SnSe	0.12	7.69	0.35	4.41,2.20
SnS	0.17	4.47	0.63	3.25,1.62
GeSe	0.13	3.18	0.51	2.66,1.33
GeS	0.21	3.14	0.82	2.65,1.32

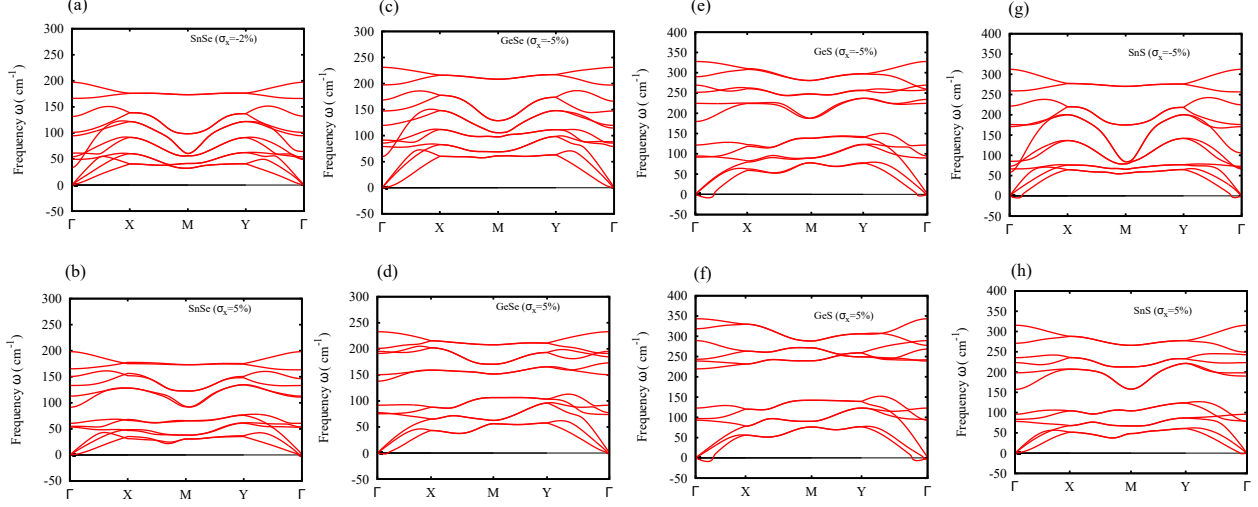


FIG. S4: Phonon band structures of considered monolayers at two extreme uniaxial strains at Γ point. We have calculated the phonon dispersion at $\sigma_x = -2\%$ in the case of SnSe because the double well structure in the free energy vanishes at a compressive strain of 2%.

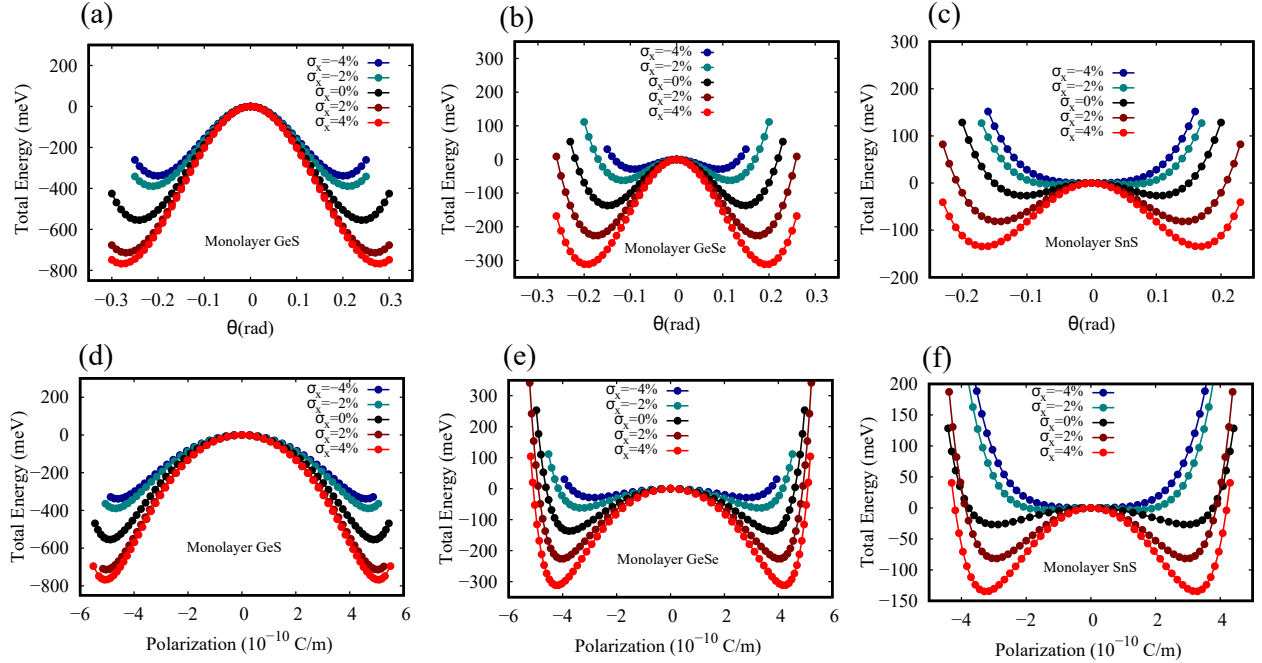


FIG. S5: Strain induced modification in the double-well potential of GeS, GeSe, and SnS monolayers as a function of (a)-(c) θ , (d)-(f) polarization.

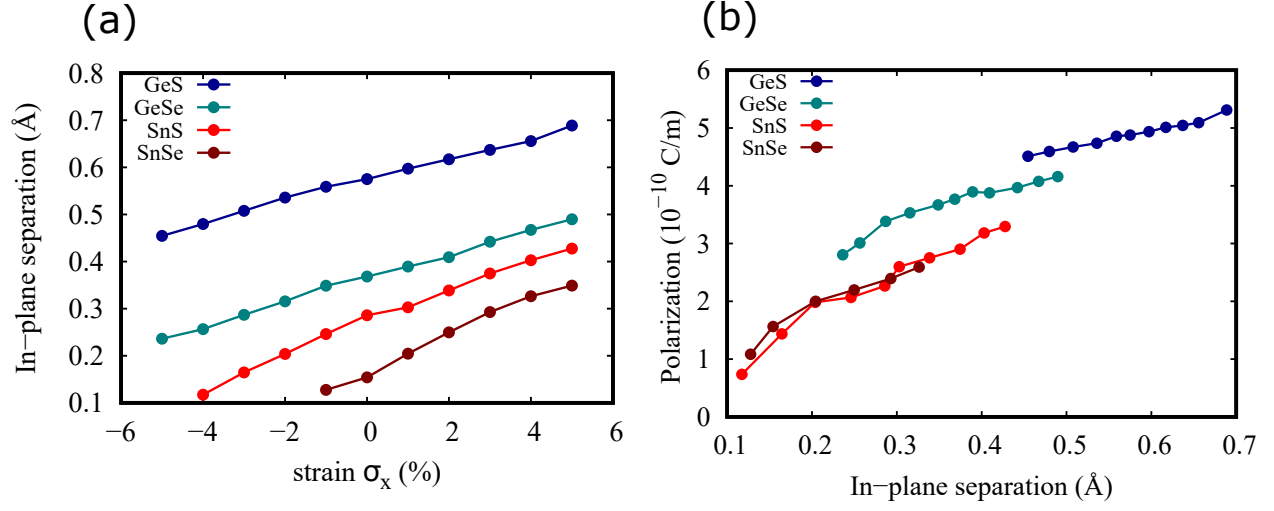


FIG. S6: (a) The change in the in-plane separation of MX (M=Ge, Sn; X=S, Se) atoms as a function of strain σ_x , and (b) Polarization as a function of in-plane separation of MX atoms in all four monolayers.

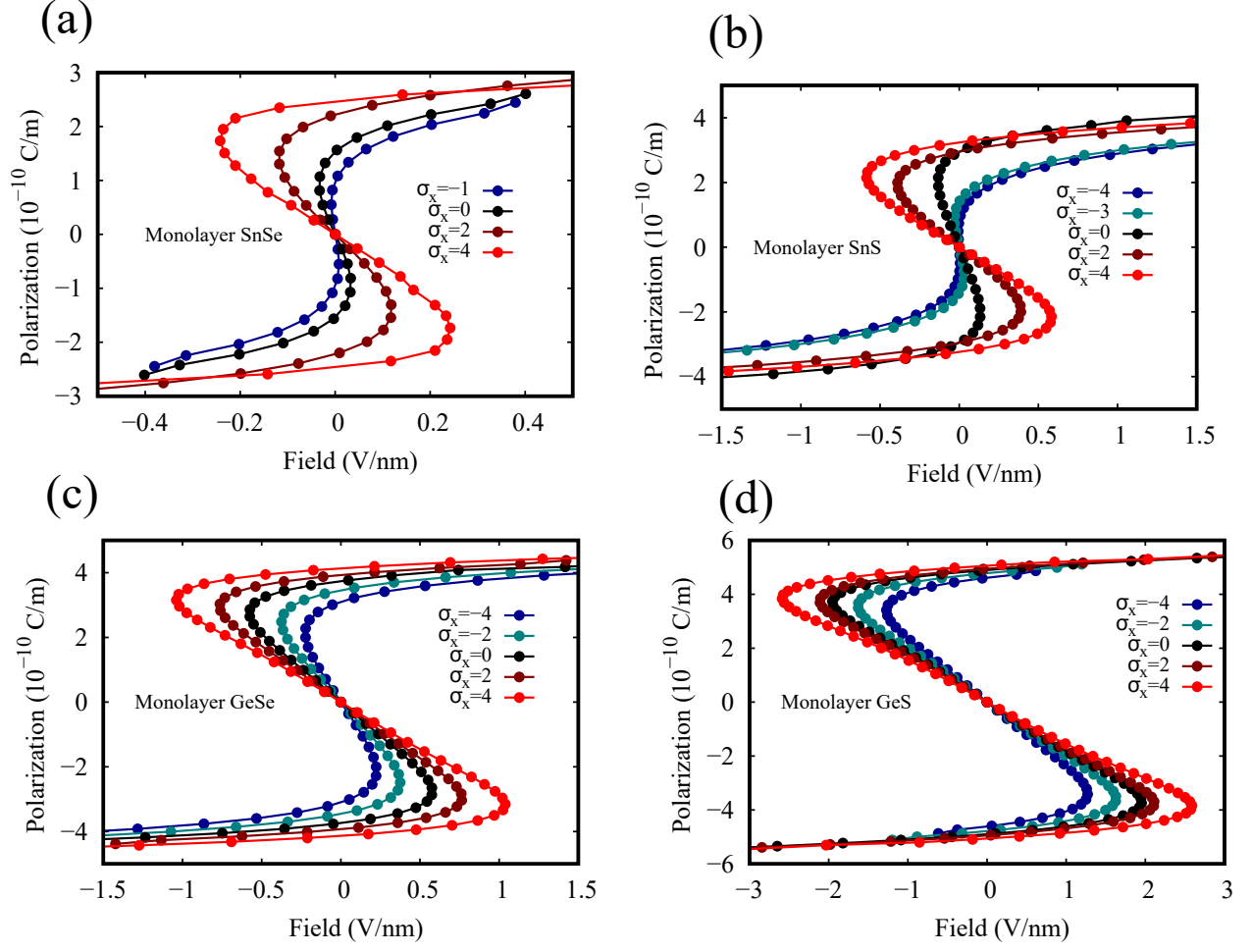


FIG. S7: The strain dependence of polarization-field curve (or S-curve) for (a) SnSe, (b) SnS, (c) GeSe, and (d) GeS, obtained using the data of Figure S5.

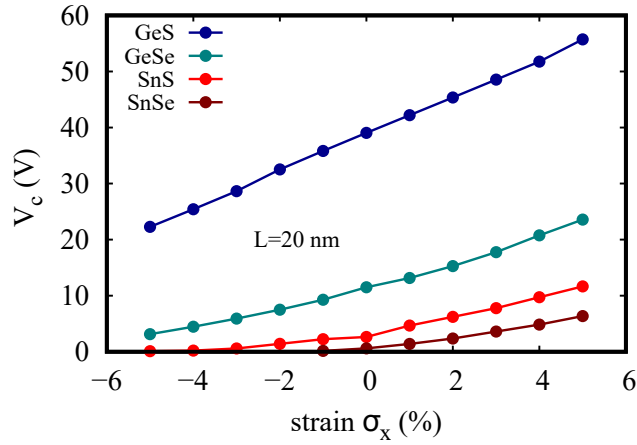


FIG. S8: The strain dependence of the coercive voltage V_C for SnSe, SnS, GeSe, and GeS monolayers, calculated using $V_C = E_c \times L$.